ADVANCED MATERIALS
www.advmat.de

A Surface Se-Substituted $LiCo[O_{2-\delta}Se_{\delta}]$ Cathode with Ultrastable High-Voltage Cycling in Pouch Full-Cells

*Zhi Zhu, Hua Wang, Yao Li, Rui Gao, Xianghui Xiao, Qipeng Yu, Chao Wang, Iradwikanari Waluyo, Jiaxin Ding, Adrian Hunt, and Ju Li**

Cycling $LiCoO_2$ to above 4.5 V for higher capacity is enticing; however, hybrid O anion- and Co cation-redox (HACR) at high voltages facilitates intrinsic $O^{\alpha-}$ ($\alpha < 2$) migration, causing oxygen loss, phase collapse, and electrolyte decomposition that severely degrade the battery cyclability. Hereby, commercial $LiCoO_2$ particles are operando treated with selenium, a well-known anti-aging element to capture oxygen-radicals in the human body, showing an "anti-aging" effect in high-voltage battery cycling and successfully stopping the escape of oxygen from $LiCoO_2$ even when the cathode is cycled to 4.62 V. Ab initio calculation and soft X-ray absorption spectroscopy analysis suggest that during deep charging, the precoated Se will initially substitute some mobile $O^{\alpha-}$ at the charged $LiCoO_2$ surface, transplanting the pumped charges from $O^{\alpha-}$ and reducing it back to O^{2-} to stabilize the oxygen lattice in prolonged cycling. As a result, the material retains 80% and 77% of its capacity after 450 and 550 cycles under 100 mA g^{-1} in 4.57 V pouch full-cells matched with a graphite anode and an ultralean electrolyte (2 g Ah^{-1}).

As the pioneer cathode for rechargeable Li-ion battery,[1] $LiCoO_2$ (LCO) is still dominating today's battery markets in consumer electronic devices, due to its high volumetric energy density and stable cycling. However, as LCO is only cycled within 4.35 V and 165 mAh g^{-1} at the present to meet the industrial-level cycling life,[2] there is still a large space to increase its utilizable capacity by charging LCO to higher voltages before it reaches its theoretical capacity of 274 mAh g^{-1}.[3] Stabilizing high-voltage LCO cycling is a hot topic in both academic and industrial research.[3,4] However, the exact mechanism that caused the quick fading of high-voltage LCO has not yet reached consensus.[5,6]

The band energy diagram in Figure S1 in the Supporting Information shows that cycling LCO to high voltage must entail a hybrid O anion ($O^{2-} \rightarrow O^{\alpha-}$, $\alpha < 2$) and Co cation-redox (HACR).[7,8] It is tempting to "exploit" HACR in LCO for much higher capacity, e.g., if LCO is charged to above 4.6 V, more than 220 mAh g^{-1} can be obtained; however, because of the reduced ionic radius and electrostatic force, the oxidized $O^{\alpha-}$ would become much mobile[9] and more likely to escape from the particle, resulting in oxygen loss (OL).

Continuous OL can be a killer problem to high-voltage cycling.[10] First, OL causes irreversible phase transformations ($CoO_2 \rightarrow Co_3O_4$)[11] (Figure S2, Supporting Information). As Co_3O_4 is a "bad" spinel with both octahedral and tetrahedral Co occupation that block Li^+ diffusion,[6] when the "densified" Co_3O_4 grows thick enough to enclose all the LCO lattices, the percolating Li^+ diffusion can be terminated, causing dramatic impedance increase. Second, as widely reported,[12,13,14] the oxygen released from the cathode, including O_2 and $O^{\alpha-}$ radicals, is highly oxidative, which could decompose the carbonate-electrolyte quickly and produce a thick cathode-electrolyte interface (CEI) that degrades battery cycling.

Therefore enabling HACR but preventing OL is the key to developing a stable high-voltage LCO cathode, and decreasing oxygen mobility at the particle surface should be the first priority. Though the use of foreign coatings was attempted in previous research,[15] few addressed the fundamental issue regarding the HACR-induced OL at high voltages, so they rarely achieved industrial-level LCO cycling at above 4.5 V, especially in graphite-anode matched full-cells. Hereby, in order to shut down OL at high voltages, we precoated commercial LCO (C-LCO) crystals with selenium (Se). As we will discuss later in this work, during high-voltage charging, the precoated Se would not only soak up the OL from the cathode to prevent it from attacking the electrolyte, but also substitute the oxidized $O^{\alpha-}$ at the charged particle surface ($Li_{1-x}CoO_2^{\alpha-} + \frac{3\delta}{2}Se \rightarrow Li_{1-x}Co[O_{2-\delta}^{2-}Se_{\delta}^{\beta+}] + \frac{\delta}{2}SeO_2$) to eliminate oxygen vacancies

Dr. Z. Zhu, Dr. H. Wang, Dr. Y. Li, Dr. R. Gao, Dr. Q. Yu, Dr. C. Wang, Prof. J. Li
Department of Nuclear Science and Engineering and Department of Materials Science and Engineering
Massachusetts Institute of Technology
Cambridge, MA 02139, USA
E-mail: liju@mit.edu
Dr. Y. Li
State Key Lab of Metal Matrix Composites
Shanghai Jiao Tong University
Shanghai 200240, China
Dr. X. Xiao, Dr. I. Waluyo, Dr. A. Hunt
National Synchrotron Light Source II
Brookhaven National Laboratory
Upton, NY 11973, USA
Dr. J. Ding
Instrumental Analysis Center
Shanghai Jiao Tong University
Shanghai 200240, China
The ORCID identification number(s) for the author(s) of this article can be found under https://doi.org/10.1002/adma.202005182.

DOI: 10.1002/adma.202005182

 © 2020 Wiley-VCH GmbH

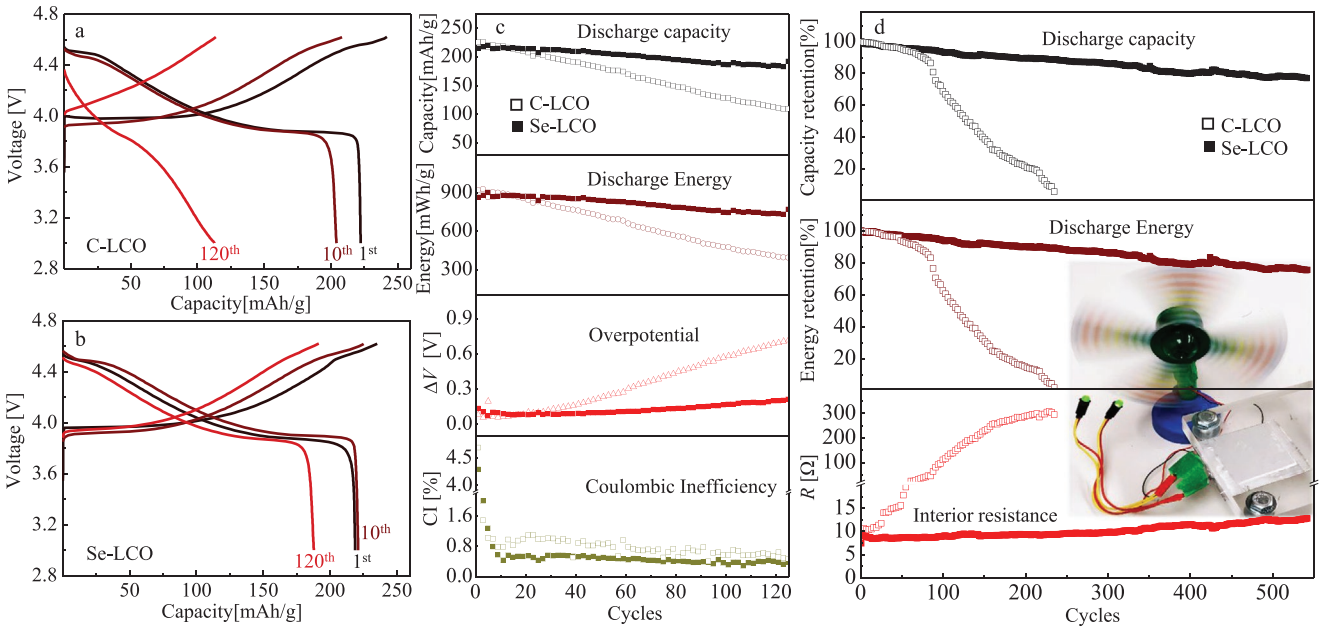

Figure 1. The electrochemical performances of C-LCO and Se-LCO cathodes in coin half-cells and pouch full-cells. a,b) The charge/discharge profiles of C-LCO (a) and Se-LCO cathode (b) within 3.0–4.62 V in coin half-cells under 70 mA g^{-1}. c) The cycling of discharge capacities, energy densities, overpotentials, and Coulombic inefficiencies of C-LCO and Se-LCO cathodes within 3.0–4.62 V in coin half-cells under 70 mA g^{-1}. d) The cycling retention of discharge capacities, energy densities, and interior resistance of C-LCO and Se-LCO pouch full-cells with graphite anodes under 100 mA g^{-1} to 4.57 V followed with floating current of 40 mAh g^{-1} again to 4.57 V and discharge to 2.95 V under 100 mA g^{-1}.

and replenish electrons ($Se \rightarrow Se^{\beta+}$) to the charged $O^{\alpha-}$ ions ($O^{\alpha-} \rightarrow O^{2-}$), reducing the mobile $O^{\alpha-}$ ions back to immobile O^{2-} at the charged particle surface, to shut down the global oxygen migration in the prolonged cycling. Se is a soft metalloid and an important antiaging element in biology[16] in the form of selenocysteine $-CH_2-SeH$ that captures the oxygen-radical species in the human body.[17] In this study, we will show that Se would also have an "antiaging" effect on the high-voltage LCO battery cycling by eliminating OL from the cathode.

In this work, we demonstrated that the surface Se-substituted LCO (Se-LCO) has greatly suppressed OL and phase collapse during high-voltage cycling. Moreover, the Se-LCO cathode also mitigated electrolyte decomposition, CEI growth, and acidic corrosion (e.g., hydrofluoric acid (HF)) to stabilize the interface kinetics. Therefore, Se-LCO displayed greatly stabilized cycling even when it was charged to 4.62 V and exhibited ultrastable high-voltage cycling in full-cells that matched with graphite anode and ultralean electrolyte (2 g Ah^{-1}). Finally, ab initio calculation and soft X-ray absorption spectroscopy (sXAS) analysis were also conducted to understand the mechanism of $Se^{\beta+}$ substitution at the oxygen anion site and the stabilization of OL during high-voltage cycling.

The C-LCO and Se-LCO electrodes were first tested in coin half-cells within 3–4.62 V, and the charge/discharge profiles in **Figure 1**a,b showed that in the 1st cycle, C-LCO was charged to 242 mAh g^{-1} and discharged to 223 mAh g^{-1} under 70 mA g^{-1}, and Se-LCO was charged to 235 mAh g^{-1}, discharged to 218 mAh g^{-1}. Though Se-LCO had slightly decreased initial capacity due to the coated Se, after 120 cycles, the voltage profile of C-LCO severely deformed, indicating a devastating high-voltage cycling degradation, but while that of Se-LCO remained very stable.

Figure 1c shows the cycling performance of C-LCO and Se-LCO within 3.0–4.62 V in half-cells under 70 mA g^{-1}. Se-LCO retained 189 mAh g^{-1} and 746 mWh g^{-1} after 120 cycles, whereas those of C-LCO decreased to 111 mAh g^{-1} and 402 mWh g^{-1}. More crucially, the overpotential ($\Delta U \equiv U_{ch} - U_{disch}$, where U_{ch} and U_{disch} are the average charge and discharge potential vs Li^+/Li) of Se-LCO ($\Delta U_{Se\text{-}LCO}$) only increased by 170 mV after 120 cycles. However, $\Delta U_{C\text{-}LCO}$ increased by 620 mV after 120 cycles, almost four times that of $\Delta U_{Se\text{-}LCO}$. The irreversible capacity in each cycle was investigated by comparing the cyclic Coulombic inefficiency (CI ≡ 100% − CE, where CE means Coulombic efficiency) in Figure 1c. The average $CI_{Se\text{-}LCO}$ was less than half of $CI_{C\text{-}LCO}$ in cycling, thus the side reactions in the Se-LCO cycling were suppressed by at least 50% in each cycle, including that from electrolyte decomposition and chemical corrosion from the side products (e.g., HF) in the electrolyte.

The C-LCO and Se-LCO cathodes were then cycled in pouch full-cells matched with graphite anodes and ultralean electrolyte (2 g Ah^{-1}) within 2.95–4.57 V under 100 mA g^{-1}. The full-cell cycling in Figure 1d showed that while the capacity and energy density of C-LCO rapidly faded to below 50% within 100 cycles and totally "died" within 250 cycles, Se-LCO stably retained 80% of its capacity (79% of energy-density) after 450 cycles and 77% of its capacity (75% of energy-density) after 550 cycles. The much poorer cycling stability of C-LCO in full-cells (Figure 1d) compared to in half-cells (Figure 1c) can be understood from the quick depletion of the lean electrolyte. In contrast, because the prevented OL from Se-LCO can help mitigate the electrolyte consumption, and moreover the carbonate-electrolyte (with $LiPF_6$ salt) has better compatibility with the graphite anode,[18] Se-LCO had even displayed much more stable high-voltage cycling in the full-cell (Figure 1d) than in the

© 2020 Wiley-VCH GmbH

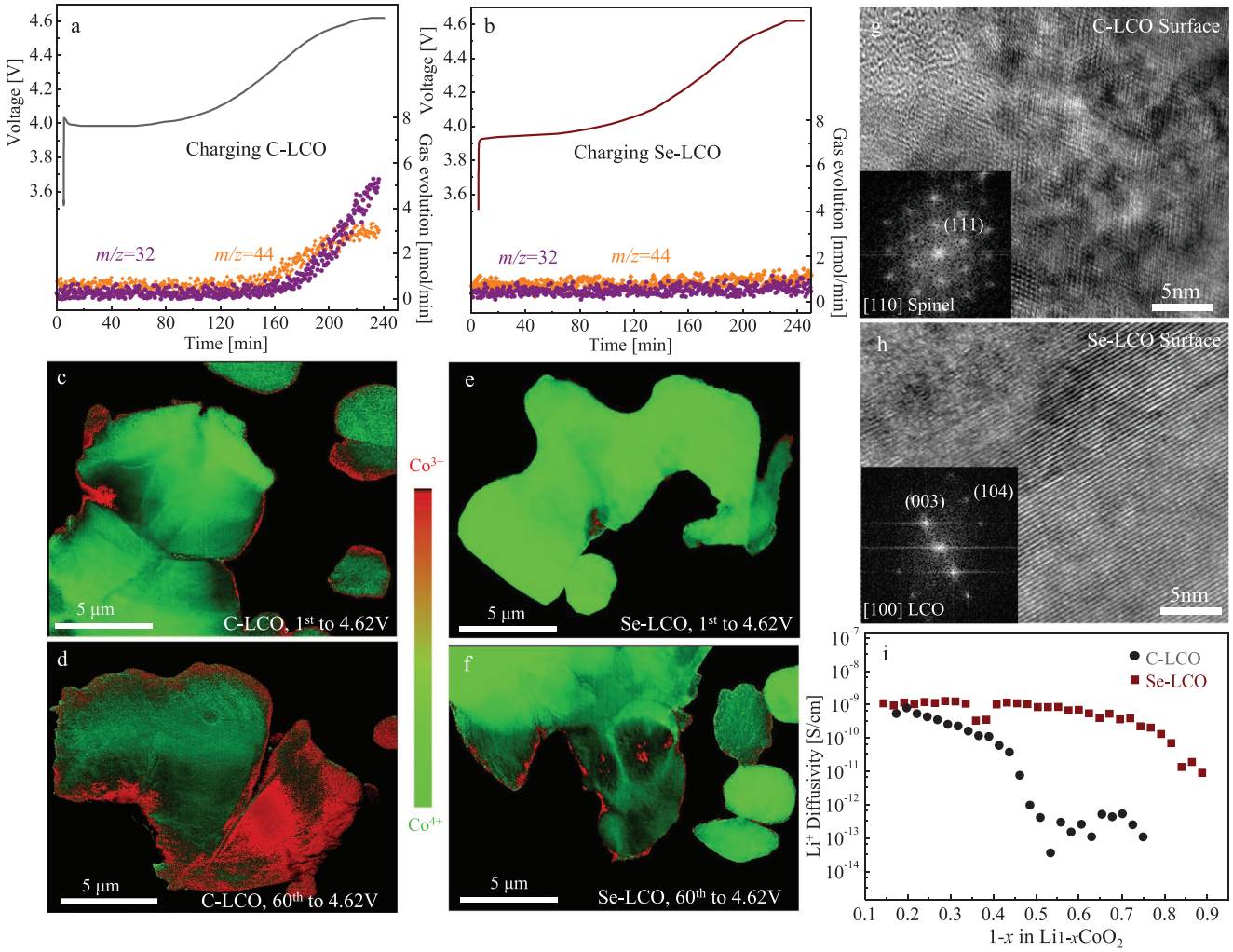

Figure 2. Tracking of oxygen release and Co reduction, and the phases and Li^+ diffusivities in the cathodes. a,b) DEMS during charging the C-LCO cathode (a) and the Se-LCO cathode (b) to 4.62 V. c–f) The Co valence mapping in the C-LCO (c,d) and Se-LCO (e,f) particles when charged to 4.62 V in the 1st (c,e) and 60th (d,f) cycles. The color scheme indicates the Co valence change from +3 (in red) to +4 (in green). g,h) The HRTEM images of the C-LCO (g) and Se-LCO (h) particles near the surface after 120 cycles and FIB preparation; insets are the FFT pattern from the HRTEM images. i) The Li^+ diffusivity within the C-LCO and Se-LCO cathodes in the 120th cycle.

half-cell (Figure 1c). This is the first time that one reported such ultrastable cycling of a prototype 4.57 V LCO pouch full-cell, so we believe this work could be a significant milestone for developing an industrial-scale high-voltage LCO battery.

Additionally, the interior resistance (R) of the full-cell was calculated by $R \equiv V/2i$, where i is the cycling current, and is shown in Figure 1d. Though C-LCO and Se-LCO had similar initial R of ≈12 Ω, while $R_{\text{C-LCO}}$ increased by ≈300 Ω after 250 cycles, $R_{\text{Se-LCO}}$ only increased by ≈5 Ω after 550 cycles, so that the average R increase of Se-LCO ($\Delta R_{\text{Se-LCO}}$) in each cycle was less than 1/100 of $\Delta R_{\text{C-LCO}}$. The stabilized R of the Se-LCO full-cell had not only maintained the applicable energy density in cycling, but would also decrease the heat generation in a practical battery pack and thus favor battery safety under high rates.

We carried out differential electrochemical mass spectroscopy (DEMS) to monitor the O_2 evolution during charging. As shown in **Figure 2**a, when C-LCO was charged to above 4.5 V, obvious O_2 and CO_2 gas began to release, confirming OL from C-LCO and the accompanying electrolyte decomposition during the high-voltage charging. However, remarkably, neither O_2 nor CO_2 evolution was detected when Se-LCO was charged to 4.62 V (Figure 2b). The DEMS results demonstrated that the oxygen-migration-induced OL and electrolyte decomposition were greatly suppressed while Se-LCO was charged to high voltage.

O_2 escape from the LCO particle must result in Co reduction,[19] where the reduced Co ions ($Co^{2+/3+}$) would migrate to the adjacent tetrahedral or octahedral sites, transforming the charged layered lattice to spinel (Co_3O_4) phase.[11] This "bad" spinel is not only electrochemically inactive, but also blocks Li^+ diffusion in cycling.[6] In this work, we performed Co X-ray absorption near edge structure (XANES) mapping at the National Synchrotron Light Source II (NSLS-II) of Brookhaven National Laboratory, to track the Co valence distribution in the charged particles. As shown in Figure 2c,d, when first charged to 4.62 V, while most of the Co in C-LCO was charged to ≈+4 valence (in green), there appeared a few patches comprising of

© 2020 Wiley-VCH GmbH

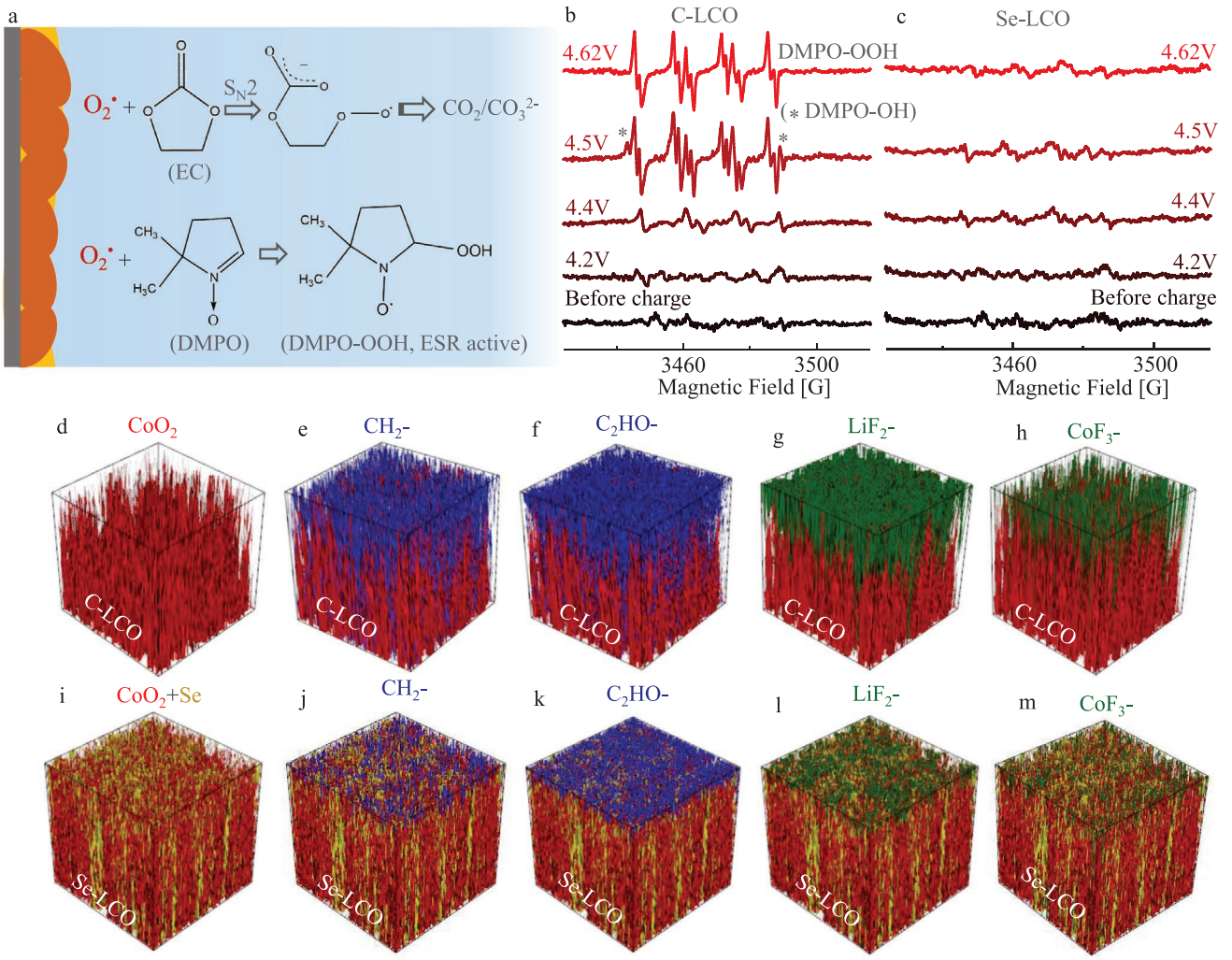

Figure 3. The prevented generation of oxygen radicals in the electrolyte and 3D cathode surface reconstruction. a) The schematic of the decomposition of the carbonate electrolyte that resulted from the production and release of oxidative oxygen radicals at high voltages. b,c) The EPR signals from the electrolytes with 10×10^{-3} M DMPO added when charging C-LCO (b) and Se-LCO (c) to different voltages. d–m) The 3D reconstruction of CoO_2^-, CH_2^-, C_2HO^-, LiF_2^-, and CoF_3^- fragment at the C-LCO (d–h) and Se-LCO (i–m) cathode surface after 120 cycles.

low-valent Co ions (≈+3, in red) at the surface, and more seriously, the charged C-LCO particle was almost fully covered by reduced Co ions after 60 cycles. However, very differently, there was very little reduced Co ions in the charged Se-LCO particle in either the 1st or 60th cycle (Figure 2e,f). The Co XANES mapping further confirmed that OL was prevented when Se-LCO was charged to a high voltage.

The suppressed OL and Co reduction, even at high voltage, could help stabilize the particle phase during the Se-LCO cycling. The scanning electron microscopy (SEM) images in Figure S3 in the Supporting Information show that while there were severe cracks and denudation shreds at the C-LCO particle surface after 120 cycles, the morphology of the Se-LCO particle remained very dense and smooth. The high-resolution transmission electron microscopy (HRTEM) images in Figure 2g,h additionally indicated that there were random spinel domains near the C-LCO particle surface, but very differently, the Se-LCO particle still has stable ordered layered lattices. The stabilized layered phase in Se-LCO can greatly maintain the bulk Li^+ diffusion and interior resistance (R) in the battery cycling (Figure 1d). The galvanostatic intermittent titration technique (GITT) in Figure S4 in the Supporting Information shows that the voltage drops in titrating Se-LCO were greatly suppressed compared to that of C-LCO in the 120th cycle. The calculated Li^+ diffusivities (D_{Li^+}) in the 120th discharge (Figure 2i) indicated that the average D_{Li^+} of Se-LCO was $\approx 10^{-9}$ S cm^{-1}, about 3 orders magnitude higher than that of C-LCO. The high D_{Li^+} of Se-LCO significantly maintained the kinetics and stabilized the cell cycling, as shown in Figure 1c,d.

As widely reported,[13,20] electrolyte decomposition can be especially aggravated when oxygen radicals[13,21] were produced in the electrolyte (e.g., hydroxyl HO• or superoxide O_2•), which can oxidize the carbonate-solvent with S_N2 attack[14] (**Figure 3**a). Electron paramagnetic resonance (EPR) spectroscopy was carried out to check the generation of oxygen radicals during charging. For higher experimental accuracy, 5,5-dimethyl-1-pyrroline *N*-oxide (DMPO) was added into the electrolyte as a radical trapper to extend these oxygen radicals' lives[22] (Figure 3a). Figure 3b,c clearly shows that the electrolyte became EPR active

 © 2020 Wiley-VCH GmbH

when C-LCO was charged to above 4.4 V. Note that the resonance curve after 4.5 V gradually built a typical six-pairs EPR signal attributed to a classical DMPO–OOH adduct, mixed with a small amount of DMPO–OH,[23] so the EPR analysis clearly suggested the generation of O_2• (with HO•) in the electrolyte when C-LCO was charged to above 4.5 V. However, the EPR response from the electrolyte when Se-LCO was charged to 4.62 V was very low and did not suggest the presence of EPR-active DMPO adducts, so we can infer that the production of oxidative oxygen radicals had been suppressed in the electrolyte when Se-LCO was charged to a high voltage.

The absence of the generation of O_2 from the Se-LCO cathode and oxygen-radicals in the electrolyte would greatly suppress CEI growth the cathode. We then performed time-of-flight secondary-ion mass spectrometry (TOF-SIMS) to analyze the cathode surface after 120 cycles (Figures S5–S7, Supporting Information) and conducted a 3D surface reconstruction. First, it can be seen that the C-LCO crystal was seriously corroded as the surface became very rough (Figure 3d), but the Se-LCO particle remained very smooth (Figure 3i), consistent with the SEM morphology in Figure S3 in the Supporting Information. Then, we used CH_2^- (Figure 3e,j) and C_2HO^- (Figure 3f,k) fragments to represent the CEI component in the 3D reconstruction.[6] The much thinner CEI layer covering on the cycled Se-LCO cathode than on the cycled Se-LCO (Figure S7, Supporting Information) demonstrated that while the carbonate-solvent was severely decomposed in the C-LCO cycling, it remained stable in the Se-LCO cycling. Additionally, the Se-LCO surface also prevented acidic corrosion from the side-products (e.g., HF) in the electrolyte, as the LiF_2^- (Figure 3l) and CoF_3^- (Figure 3m) layers at the Se-LCO cathode surface were much thinner than those at the C-LCO surface (Figure 3g,h) after 120 cycles. The much-thinner CEI layer at the Se-LCO particle surface, containing less fluoride, would greatly favor the interfacial Li^+ transfer. The EIS analysis in Figure S8 in the Supporting Information clearly indicates that the interface impedance of Se-LCO was less than 1/2 that of C-LCO (≈150 Ω) after 120 cycles. Additionally, the Co deposition at the graphite anode in the Se-LCO matched full-cell was also suppressed, compared to that cycled with C-LCO (Figure S9 and Table S1, Supporting Information), which also favored the full-cell cycling, as shown in Figure 1d.

In order to understand how the coated Se prevented OL from LCO during high-voltage cycling, we first conducted an ab initio calculation to predict the possible behaviors between the deeply charged $Li_{1-x}CoO_2$ lattice and Se. According to the first-principles density functional theory (DFT) relaxation calculation in Figure S10 in the Supporting Information, when the mobile oxidized $O^{\alpha-}$ initially leaves the deeply charged lattice (**Figure 4**a)

$$Li_{1-x}CoO_2 \rightarrow Li_{1-x}Co[O_{2-\delta}\square_\delta] + \delta O \quad (1)$$

the Se substitution on these leftover oxygen vacancy (Vo) sites in the charged lattice would be favored (Figure 4b). That is, an exchange strategy of O↔Se would be more preferable than leaving Vo in the deeply charged LCO lattice that occurred in C-LCO at high voltage, by following an operando reaction of

$$Li_{1-x}CoO_2^{\alpha-} + \frac{3\delta}{2}Se \rightarrow Li_{1-x}Co[O_{2-\delta}Se_\delta] + \frac{\delta}{2}SeO_2 \quad (2)$$

then we can get a Se-substituted lattice near the charged Se-LCO particle surface (Figure 4a,b).

In this process, the coated Se would first catch the initial escaping oxygen by forming a SeO_2 outer-layer to prohibit the escaping oxygen from reacting with the precious electrolyte. This process can be experimentally verified by the XPS analysis in Figure S11 in the Supporting Information, which showed that the precoated metallic Se was gradually oxidized to SeO_2 in the initial 10 cycles.[24] More crucially, the charge density distribution from first-principles DFT calculation, shown in Figure 4c, indicated electron transfer from Se atom to Co atom, where the Bader charge analysis in Table S2 in the Supporting Information also verified that the Se ions in the Se-substituted lattice has positive valence ($Li_{1-x}Co[O_{2-\delta}Se_\delta^{\beta+}]$). The positive $Se^{\beta+}$ in the lattice was also confirmed by the XPS depth analysis in Figure 4d, where the new Se 3p peak at ≈162.3 eV between the metallic Se (161 eV) and SeO_2 (164 eV) that appeared beneath the SeO_2 outer-layer suggested an average Se valence of $0 < \beta < 4$.[25]

DFT calculations by Lee and Persson showed that the potential energy barrier of O^{1-}–V_O exchange was 0.9 eV, while that of O^{2-}–V_O exchange was 2.3–4.0 eV.[9] Thus at room temperature ($k_BT = 0.025$ eV), oxygen migration is practically possible only if a) $\alpha < 2$, and b) there is a V_O adjacent to $O^{\alpha-}$. The role of Se in stopping the ill effects of reaction (1) can be threefold: i) the formation of SeO_2, a 1D solid polymer oxide, prevents the escaping oxygen from attacking the precious electrolyte; ii) additional Se "plugs" into the V_O sites inside the lattice near the surface, thus reducing oxygen mobility by removing one necessary condition for $O^{\alpha-}$–V_O exchange; otherwise, such V_O will be pumped back toward the interior of the ≈10 µm LCO crystal to further facilitate oxygen migration in the interior to cause continuous OL; iii) Se-substitution can transplant the pumped charges from the oxidized $O^{\alpha-}$, by replenishing electrons to the oxidized $O^{\alpha-}$ (Se–Co→O) and reducing the mobile oxidized $O^{\alpha-}$ ions back to immobile O^{2-} ions, so the other necessary condition for $O^{\alpha-}$–V_O exchange is also removed. This is accomplished by the "sacrificial" oxidation of Se (Se→$Se^{\beta+}$) in $Li_{1-x}Co[O_{2-\delta}Se_\delta^{\beta+}]$, as verified with both DFT calculation and XPS analysis. For such "sacrificial" oxidation of Se to happen, the equilibrium potential of $U^{eq}(Se^{\beta+/0})$ should be somewhat lower than $U^{eq}(O^{\alpha-/2-})$, so instead of oxygen anion-oxidation near the surface, Se is sacrificially oxidized at the high voltages, especially when there is V_O in the lattice. Additionally, the DFT calculation showed that while the substituted $Se^{\beta+}$ sat near the vacated V_O site, it was not at the V_O site exactly but was significantly elevated toward the adjacent Li layer (LiL) (Figure 4c; Figure S10, Supporting Information), and moreover, the migration energy barriers of $Se^{\beta+}$ in LiL was surprisingly small (<0.35 eV; Figure S12, Supporting Information). Thus, the highly charged LCO lattice also provides fluent kinetic pathways for the operando inward diffusion of $Se^{\beta+}$ to prevent oxygen migration.

From a crystal chemistry point of view, cation substitution of anion site would be quite unusual. However, as Figure 4c shows, $Se^{\beta+}$ was not at the V_O site exactly and was significantly elevated out of the anion plane. So we believe a more acceptable interpretation would be the formation of "selenite (SeO_3^{2-}) like" resonant structures where Se would take the formal charge of $\beta = 4+$ if oxygen is taken to be 2–, or lower-valence ($0 < \beta < 4$) analogs. So a way of looking at the LCO surface passivation

© 2020 Wiley-VCH GmbH

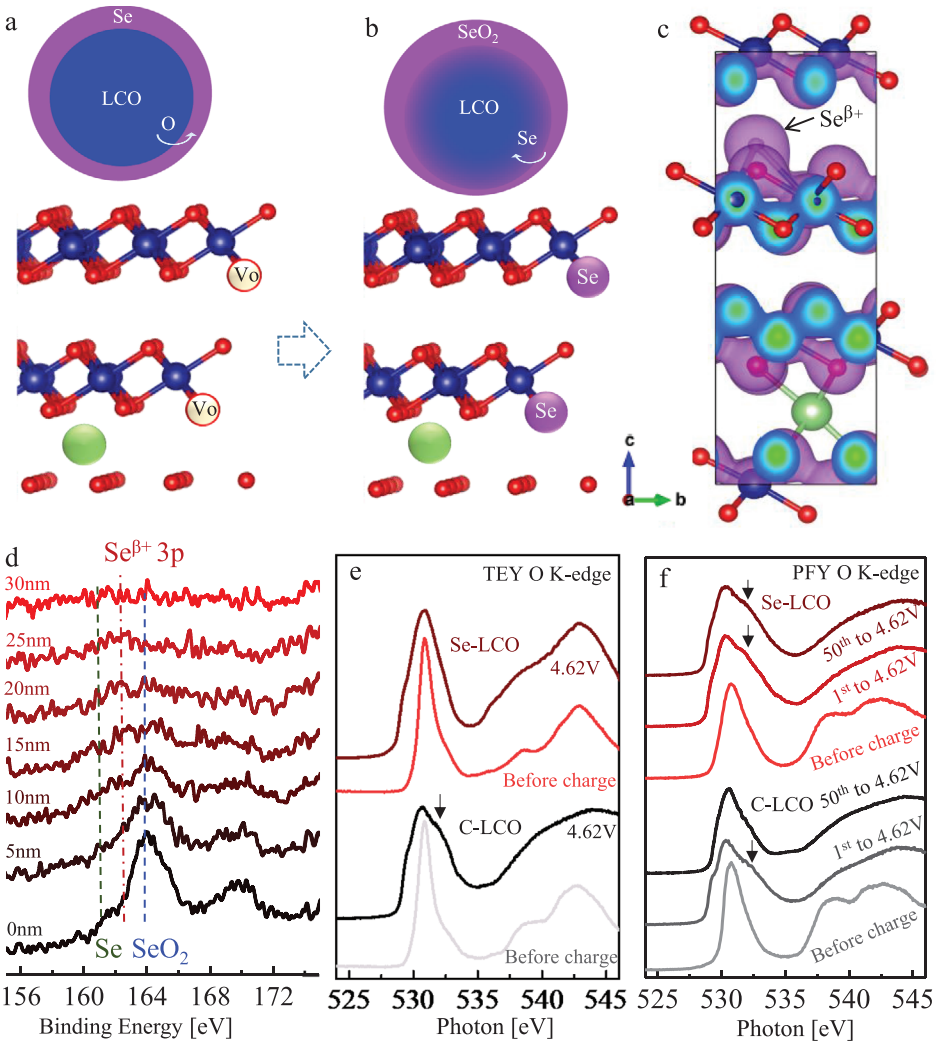

Figure 4. The Se-substitution and prevention of oxygen migration in the highly charged Se-LCO particle. a) The schematic and lattice structure when the mobile O escapes from the charged LCO lattice with leftover V_O. b) The schematic and lattice structure when Se substitutes V_O. c) The charge density distribution in the charged Se-LCO lattice from first-principles DFT calculation. d) The XPS Se 3p edge at different depths in the Se-LCO particle after 10 cycles, where the green, blue, and red dashed lines indicate the 3p location of metallic Se, SeO_2, and $Se^{\beta+}$. e,f) sXAS O K-edge spectra of C-LCO and Se-LCO under TEY mode (e) and PFY mode (f) at different states of charge.

by Se is the formation of "lithium cobalt selenite" like motifs near the surface, covered by SeO_2 on the outside. This "fixes" the HACR-induced OL, plugs the V_O and immobilizes oxygen near the surface, thus preventing further OL and V_O pumping backward into the interior, which eventually would lead to phase collapse into densified "bad spinel" Co_3O_4.[26]

sXAS was performed under TEY mode to investigate the oxidation states of oxygen ions at the charged particle surface.[27] In Figure 4e when charged to 4.62 V, while the peak intensity at ≈530 eV for C-LCO obviously decreased with a new peak appearance at +2 eV higher energy, confirming an expected $O^{2-}\rightarrow O^{\alpha-}$ reaction at the C-LCO particle surface,[8] the TEY sXAS O K-edge of Se-LCO changed very little, verifying that the oxygen ions indeed remained at −2 valence at the charged Se-LCO particle surface. The eliminated $O^{2-}\rightarrow O^{\alpha-}$ at the Se-LCO particle surface would greatly suppress the global oxygen migration and OL at high voltage,[10,28] because even though the oxygen ions in the particle bulk can still be oxidized, it was enclosed in the bulk and cannot trespass the $O^{\alpha-}$-free $Li_{1-x}Co[O_{2-\delta}Se_{\delta}]$ surface. Furthermore, there is no superabundant V_O to assist the global oxygen migration (as is well known, surfaces and grain boundaries are typical sources for lattice vacancies, and there are few grain boundaries in these large commercial LCO single crystals), then the bulk HACR ($O^{2-}\rightarrow O^{\alpha-}$) reversibility can be significantly improved in the prolonged Se-LCO cycling. The PFY sXAS O K-edge of C-LCO and Se-LCO in Figure 4f indicated that while both C-LCO and Se-LCO entailed heavy bulk oxygen anion-redox ($O^{2-}\rightarrow O^{\alpha-}$) in the 1st charging,[27] only the PFY O K-edge of Se-LCO kept unchanged after 50 cycles, as that of C-LCO showed little fingerprint of oxidized $O^{\alpha-}$ in the 50th charging.

In summary, in this work commercial LCO material was investigated when it was cycled up to 4.62 V, which showed that the percolating oxygen migration out of the particle at high

© 2020 Wiley-VCH GmbH

voltage caused irreversible phase transformation and aggravated electrolyte decomposition, leading to rapid high-voltage cycling decay. Then, these LCO crystals were coated with Se, and during deep charging, Se did not only catch the escaped oxygen from the cathode to prevent it from attacking the electrolyte, but it would also substitute part of the mobile $O^{\alpha-}$ in the charged lattice to eliminate V_O, and transplant the pumped charges $(2-\alpha)+$ from the oxidized $O^{\alpha-}$, reducing the mobile $O^{\alpha-}$ ions back to immobile O^{2-} ions, to stop the further oxygen migration. Therefore, HACR-induced OL, phase collapse, and electrolyte decomposition were significantly suppressed in the prolonged cycles to promote an ultrastable high-voltage Se-LCO cycling to the unprecedented 4.57 V in pouch full-cells with graphite anode and ultralean electrolyte (2 g Ah^{-1}), with 77% capacity retention after 550 cycles under 100 mA g^{-1}. The antiaging mechanisms of such Se modification is generic and should be applicable to other layered cathode materials such as Ni-rich and Li-rich NMC materials that involved oxygen anion-redox at high voltage to prevent OL induced issues and stabilize high-voltage and high energy density cycling.

Supporting Information

Supporting Information is available from the Wiley Online Library or from the author.

Acknowledgements

The authors acknowledge the support from the Watt Energy Technology Lab gift fund. This research used resources of the 18-ID (FXI) and 23-ID-2 (IOS) beamlines of the National Synchrotron Light Source II, a U.S. Department of Energy (DOE) Office of Science User Facility operated for the DOE Office of Science by Brookhaven National Laboratory under Contract No. DE-SC0012704. This work was performed in part at the Center for Nanoscale Systems (CNS), a member of the National Nanotechnology Coordinated Infrastructure Network (NNCI), which is supported by the National Science Foundation under NSF award no. 1541959.

Conflict of Interest

The authors declare no conflict of interest.

Keywords

cathode materials, global oxygen migration, high-voltage cycling, hybrid redox, Li-ion batteries, lithium cobalt oxides

Received: July 30, 2020
Revised: October 5, 2020
Published online: November 10, 2020

[1] K. Mizushima, P. C. Jones, P. J. Wiseman, J. B. Goodenough, *Solid State Ionics* **1981**, *3–4*, 171.
[2] S. Kalluri, M. Yoon, M. Jo, S. Park, S. Myeong, J. Kim, S. X. Dou, Z. P. Guo, J. Cho, *Adv. Energy Mater.* **2017**, *7*, 1601507.
[3] Q. Liu, X. Su, D. Lei, Y. Qin, J. G. Wen, F. M. Guo, Y. M. A. Wu, Y. C. Rong, R. H. Kou, X. H. Xiao, F. Aguesse, J. Bareno, Y. Ren, W. Q. Lu, Y. X. Li, *Nat. Energy* **2018**, *3*, 936.
[4] a) J. N. Zhang, Q. H. Li, C. Y. Ouyang, X. Q. Yu, M. Y. Ge, X. J. Huang, E. Y. Hu, C. Ma, S. F. Li, R. J. Xiao, W. L. Yang, Y. Chu, Y. J. Liu, H. G. Yu, X. Q. Yang, X. J. Huang, L. Q. Chen, H. Li, *Nat. Energy* **2019**, *4*, 594; b) J. W. Qian, L. Liu, J. X. Yang, S. Y. Li, X. Wang, H. L. L. Zhuang, Y. Y. Lu, *Nat. Commun.* **2018**, *9*, 4918.
[5] a) A. Van der Ven, M. K. Aydinol, G. Ceder, G. Kresse, J. Hafner, *Phys. Rev. B* **1998**, *58*, 2975; b) H. Xia, L. Lu, Y. S. Meng, G. Ceder, *J. Electrochem. Soc.* **2007**, *154*, A337; c) M. D. Radin, S. Hy, M. Sina, C. C. Fang, H. D. Liu, J. Vinckeviciute, M. H. Zhang, M. S. Whittingham, Y. S. Meng, A. Van der Ven, *Adv. Energy Mater.* **2017**, *7*, 1602888; d) T. Ohzuku, A. Ueda, *J. Electrochem. Soc.* **1994**, *141*, 2972; e) H. Wang, Y. I. Jang, B. Huang, D. R. Sadoway, Y. M. Chiang, *J. Electrochem. Soc.* **1999**, *146*, 473.
[6] M. Yoon, Y. Dong, Y. Yoo, S. Myeong, J. Hwang, J. Kim, S.-H. Choi, J. Sung, S. J. Kang, J. Li, J. Cho, *Adv. Funct. Mater.* **2019**, *30*, 1907903.
[7] a) Z. Zhu, A. Kushima, Z. Y. Yin, L. Qi, K. Amine, J. Lu, J. Li, *Nat. Energy* **2016**, *1*, 16111; b) Y. Qiao, K. Jiang, H. Deng, H. Zhou, *Nat. Catal.* **2019**, *2*, 1035; c) S. Venkatraman, Y. Shin, A. Manthiram, *Electrochem. Solid-State Lett.* **2003**, *6*, A9.
[8] a) W. S. Yoon, K. B. Kim, M. G. Kim, M. K. Lee, H. J. Shin, J. M. Lee, J. S. Lee, C. H. Yo, *J. Phys. Chem. B* **2002**, *106*, 2526; b) W. S. Yoon, K. B. Kim, M. G. Kim, M. K. Lee, H. J. Shin, J. M. Lee, *J. Electrochem. Soc.* **2002**, *149*, A1305.
[9] a) P. F. Yan, J. M. Zheng, Z. K. Tang, A. Devaraj, G. Y. Chen, K. Amine, J. G. Zhang, L. M. Liu, C. M. Wang, *Nat. Nanotechnol.* **2019**, *14*, 602; b) E. Lee, K. A. Persson, *Adv. Energy Mater.* **2014**, *4*, 1400498.
[10] Z. Zhu, D. Yu, Z. Shi, R. Gao, X. Xiao, I. Waluyo, M. Ge, Y. Dong, W. Xue, G. Xu, *Energy Environ. Sci.* **2020**, *13*, 1865.
[11] M. Yoon, Y. Dong, Y. Yoo, S. Myeong, J. Hwang, J. Kim, S. H. Choi, J. Sung, S. J. Kang, J. Li, *Adv. Funct. Mater.* **2020**, *30*, 1907903.
[12] a) X. Zuo, C. Fan, X. Xiao, J. Liu, J. Nan, *J. Power Sources* **2012**, *219*, 94; b) S. A. Delp, O. Borodin, M. Olguin, C. G. Eisner, J. L. Allen, T. R. Jow, *Electrochim. Acta* **2016**, *209*, 498.
[13] N.-S. Choi, J.-G. Han, S.-Y. Ha, I. Park, C.-K. Back, *RSC Adv.* **2015**, *5*, 2732.
[14] V. S. Bryantsev, M. Blanco, *J. Phys. Chem. Lett.* **2011**, *2*, 379.
[15] a) L. de Biasi, B. Schwarz, T. Brezesinski, P. Hartmann, J. Janek, H. Ehrenberg, *Adv. Mater.* **2019**, *31*, 1900985; b) S. Kalluri, M. Yoon, M. Jo, S. Park, S. Myeong, J. Kim, S. X. Dou, Z. P. Guo, J. Cho, *Adv. Energy Mater.* **2017**, *7*, 1601507; c) A. Yano, M. Shikano, A. Ueda, H. Sakaebe, Z. Ogumi, *J. Electrochem. Soc.* **2017**, *164*, A6116.
[16] Y. Zhang, Y. J. Roh, S. J. Han, I. Park, H. M. Lee, Y. S. Ok, B. C. Lee, S. R. Lee, *Antioxidants* **2020**, *9*, 383.
[17] H. Steinbrenner, H. Sies, *Biochim. Biophys. Acta, Gen. Subj.* **2009**, *1790*, 1478.
[18] K. Xu, *Chem. Rev.* **2004**, *104*, 4303.
[19] S.-M. Bak, Z. Shadike, R. Lin, X. Yu, X.-Q. Yang, *NPG Asia Mater.* **2018**, *10*, 563.
[20] a) J. Li, C. Ma, M. Chi, C. Liang, N. J. Dudney, *Adv. Energy Mater.* **2015**, *5*, 1401408; b) L. Hu, Z. Zhang, K. Amine, *J. Power Sources* **2013**, *236*, 175; c) M. Hu, X. Pang, Z. Zhou, *J. Power Sources* **2013**, *237*, 229.
[21] a) S. A. Freunberger, Y. Chen, Z. Peng, J. M. Griffin, L. J. Hardwick, F. Bardé, P. Novák, P. G. Bruce, *J. Am. Chem. Soc.* **2011**, *133*, 8040; b) H. Wang, K. Xie, *Electrochim. Acta* **2012**, *64*, 29; c) H. Wang, E. Rus, T. Sakuraba, J. Kikuchi, Y. Kiya, H. D. Abruña, *Anal. Chem.* **2014**, *86*, 6197.
[22] a) J.-L. Clément, N. Ferré, D. Siri, H. Karoui, A. Rockenbauer, P. Tordo, *J. Org. Chem.* **2005**, *70*, 1198; b) R. Cao, E. D. Walter, W. Xu, E. N. Nasybulin, P. Bhattacharya, M. E. Bowden, M. H. Engelhard, J. G. Zhang, *ChemSusChem* **2014**, *7*, 2436.

 © 2020 Wiley-VCH GmbH

[23] K. P. Madden, H. Taniguchi, *Free Radical Biol. Med.* **2001**, *30*, 1374.
[24] a) A. J. Green, S. Dey, Y. Q. An, B. O'Brien, S. O'Mullane, B. Thiel, A. C. Diebold, *J. Vac. Sci. Technol., A* **2016**, *34*, 061403; b) X. Huang, Y. Liu, C. Liu, J. Zhang, O. Noonan, C. Yu, *Chem. Sci.* **2018**, *9*, 5178.
[25] M. Gui, J. K. Papp, A. S. Colburn, N. D. Meeks, B. Weaver, I. Wilf, D. Bhattacharyya, *J. Membr. Sci.* **2015**, *488*, 79.
[26] Y. Huang, Y. Dong, S. Li, J. Lee, C. Wang, Z. Zhu, W. Xue, Y. Li, J. Li, *Adv. Energy Mater.* **2020**, https://doi.org/10.1002/aenm.202000997.
[27] R. Qiao, L. A. Wray, J.-H. Kim, N. P. Pieczonka, S. J. Harris, W. Yang, *J. Phys. Chem. C* **2015**, *119*, 27228.
[28] a) Z. Zhu, D. Yu, Y. Yang, C. Su, Y. Huang, Y. Dong, I. Waluyo, B. Wang, A. Hunt, X. Yao, *Nat. Energy* **2019**, *4*, 1049; b) Z. Zhu, R. Gao, I. Waluyo, Y. Dong, A. Hunt, J. Lee, J. Li, *Adv. Energy Mater.* **2020**, *10*, 2001120.

© 2020 Wiley-VCH GmbH

© 2020 Wiley-VCH GmbH

ADVANCED MATERIALS

Supporting Information

for *Adv. Mater.*, DOI: 10.1002/adma.202005182

A Surface Se-Substituted $LiCo[O_{2\#\#}Se_{\#}]$ Cathode with Ultrastable High-Voltage Cycling in Pouch Full-Cells

*Zhi Zhu, Hua Wang, Yao Li, Rui Gao, Xianghui Xiao, Qipeng Yu, Chao Wang, Iradwikanari Waluyo, Jiaxin Ding, Adrian Hunt, and Ju Li**

Supplementary Information

A Surface Se-Substituted $LiCo[O_{2-\delta}Se_{\delta}]$ Cathode with Ultrastable High-Voltage Cycling in Pouch Full-Cells

Zhi Zhu, Hua Wang, Yao Li, Rui Gao, Xianghui Xiao, Qipeng Yu, Chao Wang, Iradwikanari Waluyo, Jiaxin Ding, Adrian Hunt and Ju Li*

Z Zhu, H Wang, Y Li, R Gao, Q Yu, C Wang and J Li (*Corresponding author. Email: liju@mit.edu (J.Li))
Department of Nuclear Science and Engineering and Department of Materials Science and Engineering, Massachusetts Institute of Technology, Cambridge, MA 02139, USA.
X Xiao, I Waluyo, A Hunt
National Synchrotron Light Source II, Brookhaven National Laboratory, Upton, NY 11973, USA.
Y Li
State Key Lab of Metal Matrix Composites, Shanghai Jiao Tong University, Shanghai 200240, China.
J Ding
Instrumental Analysis Center, Shanghai Jiao Tong University, Shanghai 200240, China.

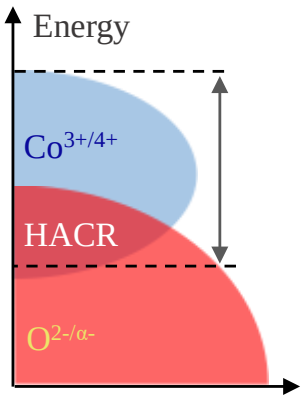

Supplementary Fig. 1 The band structures in $LiCoO_2$ and the Fermi levels during the high voltage cycling, which showed that a hybrid oxygen anion redox and Co cation redox (HACR) can be entailed when charging $LiCoO_2$ to high voltage.

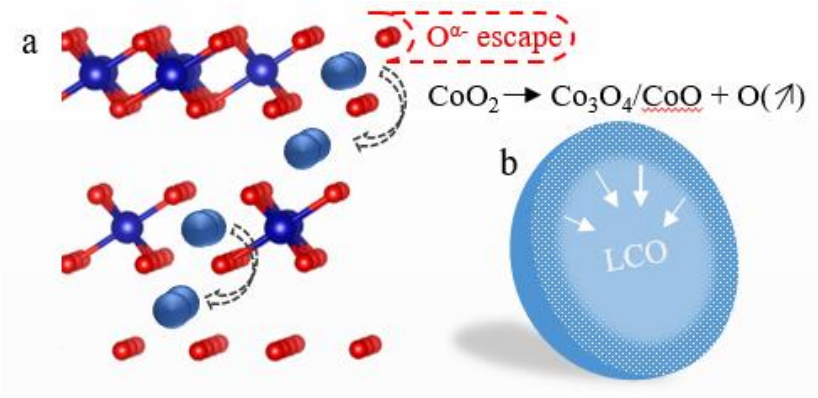

Supplementary Fig. 2 (a) The schematic of irreversible phase transformation when oxygen escaping from the lattice during the high-voltage charging. (b) The spreading of phase transformation from the charged particle surface into the particle bulk with continuous oxygen loss in the prolonged high voltage cycles.

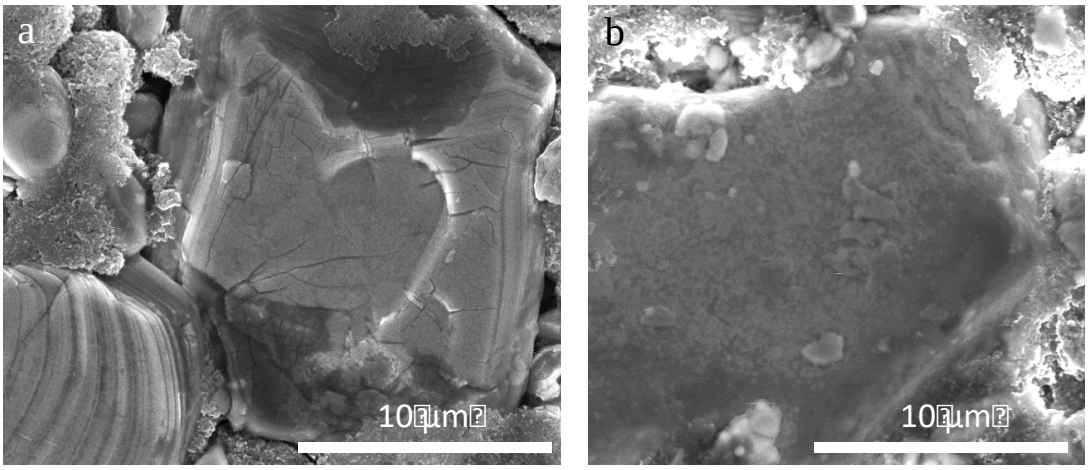

Supplementary Fig. 3 The SEM image of the C-LCO electrode (a) and Se-LCO electrode (b) after 120 cycles. The SEM images showed clear cracks and denudation shreds at the C-LCO particle surface, but the morphology of the Se-LCO particles kept very dense and smooth without cracks.

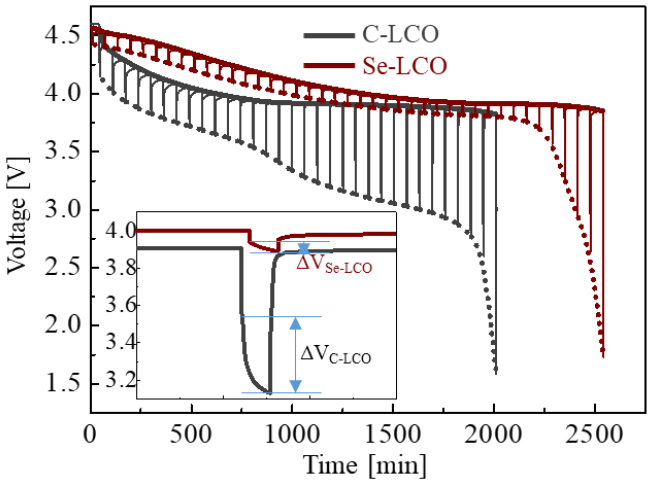

Supplementary Fig. 4 The GITT curve while discharging C-LCO and Se-LCO in the 120th cycle in the coin half-cells.

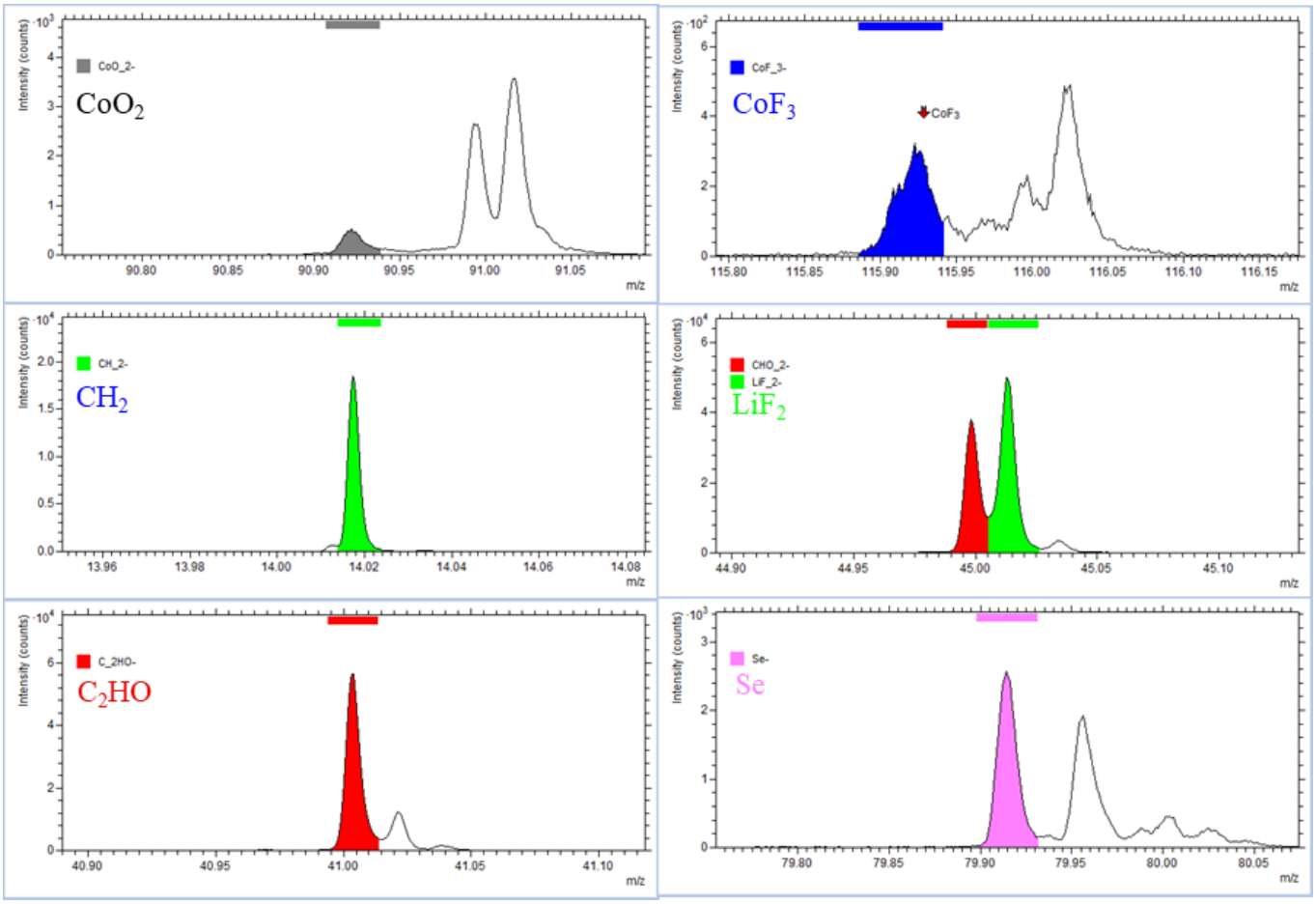

Supplementary Fig. 5 TOF-SIMS spectra of selected fragments representing the basic electrode component, fluoride compound and carbonate-based electrolyte decomposition products on C-LCO and Se-LCO electrodes after 120 cycles at 25°C.

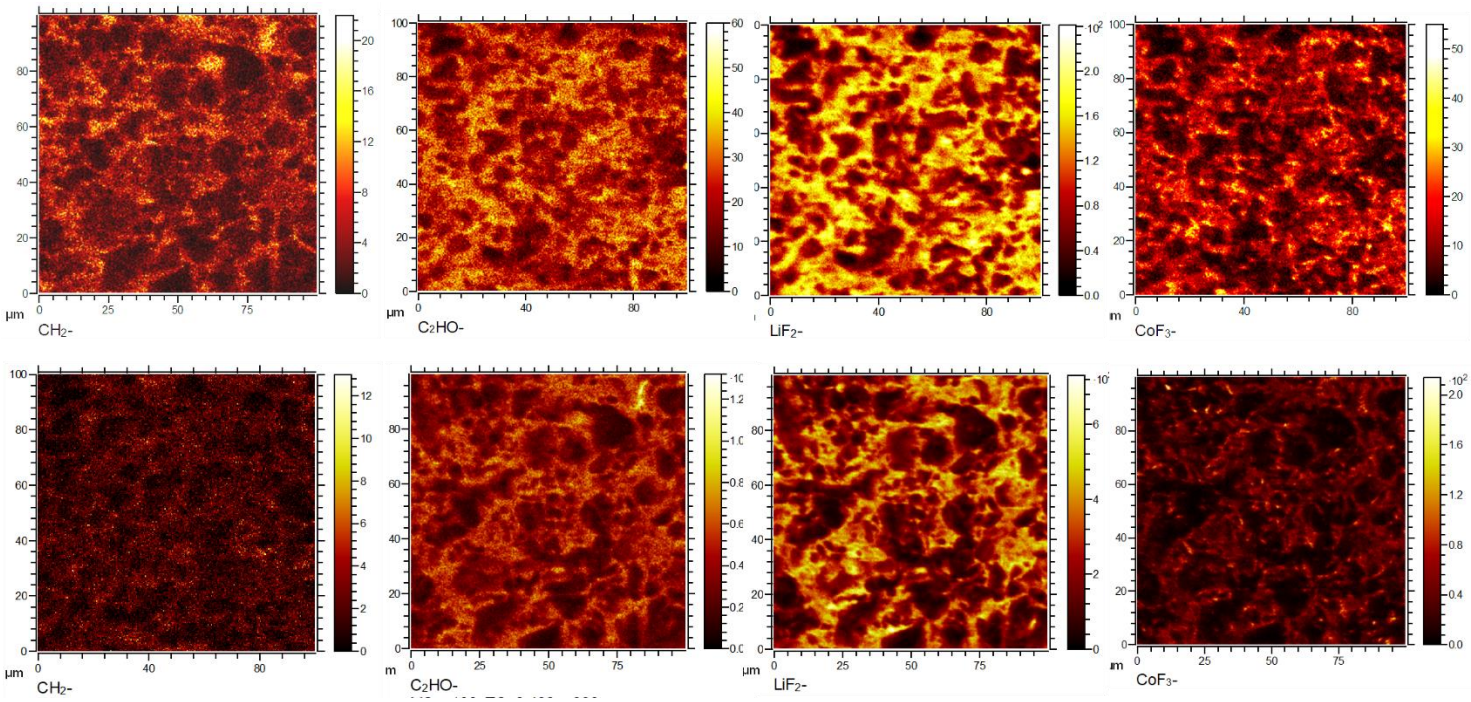

Supplementary Fig. 6 Top view TOF-SIMS image of selected fragments on the surface of C-LCO

(top) and Se-LCO (bottom) cathode after 120 cycles

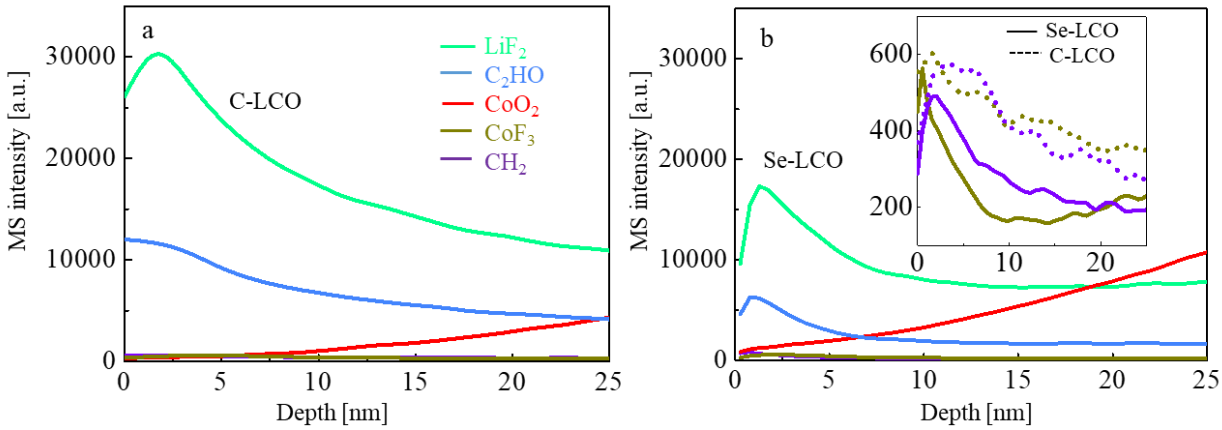

Supplementary Fig. 7 The MS signals of the CoO_2-, CH_2-, C_2HO-, LiF_2- and CoF_3- components at different depth of the C-LCO (a) and Se-LCO (b) cathode.

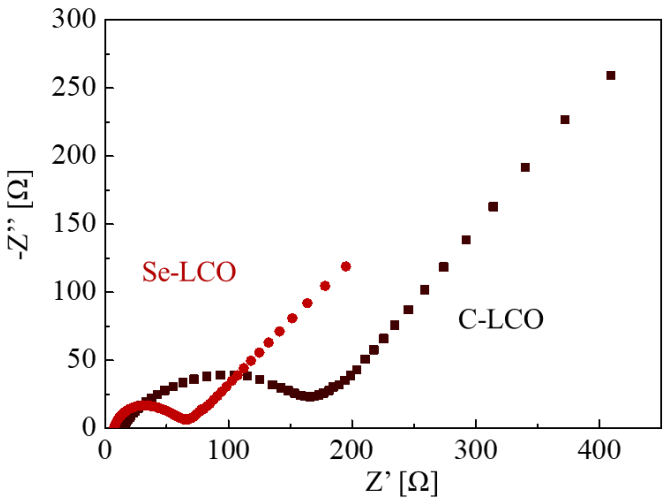

Supplementary Fig. 8 EIS curves for C-LCO and Se-LCO cathodes in the 120th cycle. From the EIS result, it can be clearly seen that R_{ct} of C-LCO was about 150 Ω while that of Se-LCO was only about 60 Ω after 120 cycles.

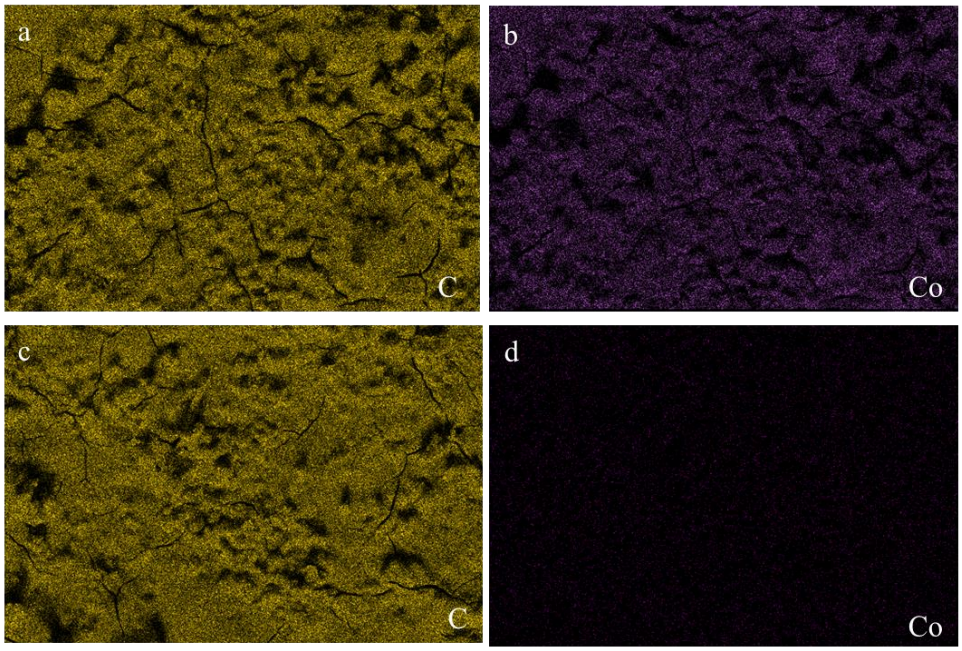

Supplementary Fig. 9 (a,b) The EDX mapping of C (a) and Co (b) at the graphite anode after 200 cycles in the full-cell with C-LCO cathode. (c,d) The EDX mapping of C (c) and Co (d) at the graphite anode after 200 cycles in the full-cell with Se-LCO cathode.

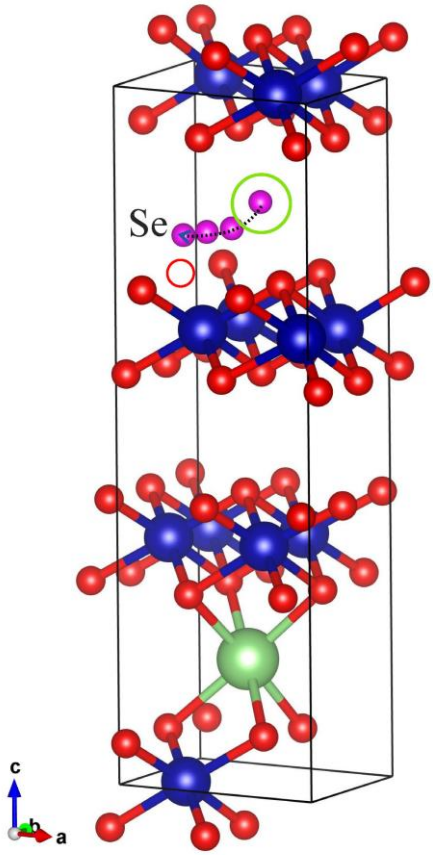

Supplementary Fig. 10 The DFT relaxation calculation in a relaxed $LiCo_{12}O_{23}Se$. The initial position of Se atom was set to Li vacancy denoted by a green circle and finally relaxed to the position around O vacancy (Wyckoff position: 6c) denoted by a red circle. The arrow indicates the relaxation path with the

Se atom.

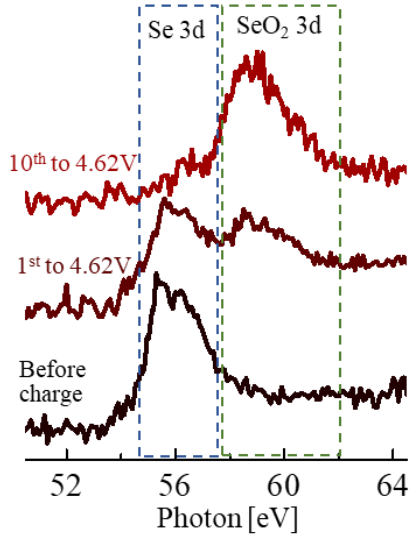

Supplementary Fig. 11 The changes of XPS Se 3d edge during the initial 10 high-voltage cycles, indicating the oxidation process of the outermost layer from metallic Se to SeO_2 in the initial cycles.

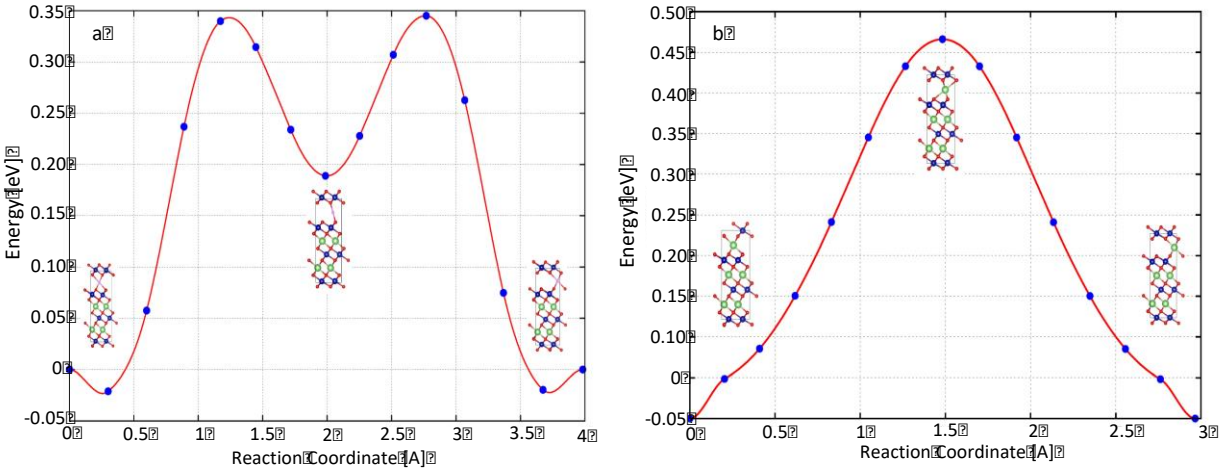

Supplementary Fig. 12 The diffusion energy barriers for Se (a) and Li (b) atoms displacement along one Li vacancy site to the next nearest Li vacancy site in the Li layer using nudged elastic band method with DFT. The initial, intermediate, and final structures are attached.

Supplementary Table 1 The content of Co at the graphite anodes disassembled from the pouch full-cells after 200 cycles. Three parts (each was 1 cm^3) were measured with ICP-AES for each graphite foil that was all immersed in 65% HNO_3 solution for 7 days.

	C-LCO	Se-LCO
1	82.3	25.1
2	74.7	19.6
3	90.2	20.3
Average	82.4	21.7

Supplementary Table 2 The relaxed coordinates of each atom, the Bader charge, the minimum distance to the zero-flux surface, and the atomic volume in $LiCo_{12}O_{23}Se$.

Atom	X	Y	Z	Charge	Minimum Distance	Atomic Volume
Li	0.704510	2.900503	2.371688	0.007015	0.271254	0.311533
Co	2.142790	3.585038	14.028112	7.385607	0.703860	6.649232
Co	-2.113527	4.515209	4.742885	7.356965	0.704627	6.663420
Co	4.968309	0.449510	9.282851	7.549126	0.709782	6.983899
Co	3.522550	1.198550	14.074773	7.378889	0.720208	6.743617
Co	-0.692618	2.062894	4.794578	7.363659	0.722375	6.553304
Co	3.522547	2.836219	9.226970	7.365616	0.719955	6.540966
Co	-0.733770	3.585038	14.028112	7.384159	0.712335	6.647073
Co	0.704513	4.475424	4.797903	7.365778	0.721818	6.573662
Co	2.076791	0.449510	9.282851	7.555136	0.723835	7.036335
Co	0.704507	1.172507	0.023239	7.380582	0.701785	6.408642
Co	2.101644	2.062894	4.794578	7.364392	0.714048	6.563483
Co	0.704507	2.791398	9.284795	7.557137	0.729902	7.010734
O	4.945271	0.379145	13.160448	6.875850	0.887924	11.552334
O	2.138763	3.644543	10.199141	6.862281	0.898219	12.109702
O	2.089923	3.672290	3.802639	6.956342	0.901466	13.233689
O	-2.113530	4.399210	0.903051	6.849794	0.895824	12.884217
O	-2.113530	4.487887	8.356519	6.847413	0.871903	12.183421
O	4.943597	0.428875	5.682817	6.833088	0.891126	12.172934
O	3.522550	2.774059	13.080670	6.879013	0.885165	12.680949
O	3.522550	1.250411	10.221653	6.871353	0.901858	12.114945
O	3.522550	1.238861	3.892449	6.839352	0.882233	12.853063
O	-0.696498	2.004228	0.954521	6.950718	0.898295	13.199760
O	-0.692778	2.030750	8.317958	6.854314	0.878814	12.246961
O	3.522550	2.898411	5.644190	6.824852	0.875343	12.001744
O	2.099829	0.379145	13.160448	6.875943	0.891142	11.584413
O	-0.729743	3.644543	10.199141	6.862058	0.893570	12.083483
O	-0.680903	3.672290	3.802639	6.957265	0.901879	13.244176
O	0.704513	4.387281	0.868542	6.956991	0.893708	13.166756
O	0.704510	4.468698	8.415339	6.768777	0.885656	12.149183
O	2.101497	0.428875	5.682817	6.834239	0.873725	12.180028
O	0.704510	2.763522	13.124742	6.892997	0.901747	11.553877
O	0.704510	1.287169	3.785507	6.961038	0.904783	13.217958
O	2.105524	2.004228	0.954521	6.949702	0.910770	13.174775
O	2.101804	2.030750	8.317958	6.852891	0.870380	12.232464
O	0.704507	2.866315	5.741951	6.856773	0.895080	12.283975
Se	0.704510	1.221959	11.048204	**5.772900**	1.193872	20.127521

Supplementary Methods

Materials preparation

The commercial $LiCoO_2$ particles (C-LCO) were ordered from *Targray Corp Lt,d.* (https://www.targray.com/li-ion-battery/cathode-materials/cathode-active-materials). The metallic selenium (Se) was ordered from Sigma-Aldrich (powder, 100 mesh, 99.99% trace metals basis). The metallic Se was firstly milled in ethanol, and then mixed with the C-LCO powders with weight ratio of 1:99. Then the mixed powder was pressed into a round pallet under 20 ton and heated in an air furnace at 240~260 ^{o}C for 8 h. Finally, the sample was cooled down with furnace and milled to powders to be the Se-LCO cathode material.

Electrochemical test

The cathode electrode was made of 95 wt% active material, 3 wt% carbon black, and 2 wt% polyvinylidene fluoride (PVDF) binder, which was pasted on an Al current collector and compressed under 20MPa. R2032 coin cells were fabricated with the above cathode, Li metal anode, a Celgard 2400 polymeric separator and a commercial electrolyte solution of 1.2 M $LiPF_6$ dissolved in a mixture of EC and DEC with a volume ratio of 1:1. Pouch full-cells were fabricated with the above cathodes, commercial graphite anode (double-side coated), a separator of Celgard 2400 polymer and a commercial electrolyte solution of 1.2 M $LiPF_6$ dissolved in a mixture of EC and DEC with a volume ratio of 1:1, and 2 wt% vinylene carbonate additive (ordered from *Soulbrain MI*). The loading density of LCO cathode was 16-17 mg/cm^2 with ~3.5 mAh/cm^2 (tested in half-cell under 0.1C); The commercial graphite anode had a loading density of ~12 mg/cm^2 with ~3.8 mAg/cm^2 (tested in half-cell under 0.1C). The pouch full cells were fabricated with double layers of electrodes (one graphite anode foil with double-sides coated and two LCO cathode foils with single-side coated). The amount of electrolyte added was about 2g/Ah in the pouch cell. A LAND CT2001A 8-channel automatic battery test system (Wuhan Lanhe Electronics) was used for charging/discharging of the cells. An electrochemical workstation (Gamry Instr, Reference 3000) was used for the galvanostatic intermittent titration technique (GITT) with constant current for 200 seconds followed with 1800 seconds relaxation until 2V. The electrochemical tests were all carried out at room temperature. A self-made quantitative DEMS was used to detect and analyze the gas during the cell testing. Two glued polyether ether ketone (PEEK) capillary tubes were used as inlet and outlet of gas. The cell was fabricated in a glove box where O_2 <0.1 ppm. Then, the output tube was connected to a Thermo Scientific mass spectrometer (MS). High-purity Ar gas was used as the carrier gas with a flow rate of 3 mL/min during the cycling process. In the constant current charging process, the current was 60 mA/g, and MS spectra were collected every 30 seconds.

Material characterizations

X-ray diffraction was performed on a PANalytical X'Pert PRO X-ray diffractor using Cu target under 45 kV, 40 mA. The data was collected with 2°/min and analyzed with the HighScore Plus software. Scanning electron microscopy was performed on a Zeiss Merlin high-resolution scanning electron microscope with X-ray spectroscopy (EDS). The high angle annular dark field (HAADF) images, energy dispersive X-ray spectroscopy (EDS) and electron energy loss spectroscopy (EELS) spectra are acquired from JEOL ARM 200F scanning transmission electron microscope (STEM) operated at 200 keV, equipped with a cold field emission gun and integrated aberration (Cs) corrector. Dual EELS spectrometers are used to collect both the low-loss and high-loss spectra, and the low-loss spectra are utilized to correct the drift of the zero-loss peak (ZLP). Based on the full-width at half-maximum (FWHM) of the zero-loss peak (ZLP), the optimal energy-resolution of EELS is about 1 eV. The STEM sample is prepared using the FEI Helios NanoLab 600 DualBeam FIB/SEM equipped with Ga ion source. A Pt layer is deposited on top to protect the cathode particle. High-resolution transmission electron microscopy (HRTEM) images and selected area electron diffraction (SAED) patterns were taken on a JEOL 2010F transmission electron microscope operated at 200KV.

Co XANES mapping

The XANES measurements of the electrode particles were conducted with a transmission X-ray microscope (TXM) at Full-field X-ray Imaging beamline of National Synchrotron Light Source II (NSLS-II) at Brookhaven National Laboratory. The XANES images were Co K-edge energy. XANES

images were acquired at different X-ray energies across the Co absorption K-edge (7.588–8.153 keV, 1 eV interval). The effective pixel size of each image is 21 nm. Standard samples ($LiCoO_2$) were used to extract the reference absorption spectra for Co^{3+} oxidation states. The whiteline peaks at each pixel in the XANES map were fitted, and the peak positions were determined as the maxima of the peaks. The images in Fig 2c-f were colored by imageJ, basing on the whiteline images.

Time-of-flight secondary-ion mass spectrometry (TOF-SIMS)

For the time-of-flight secondary-ion mass spectrometry (TOF-SIMS) studies, ION-TOF TOF-SIMS 5 was used under the pressure of analysis chamber below 1.1×10^{-9} mbar at Instrument Analysis Centre, Shanghai Jiaotong University. The organic imaging with delay extraction mode with pulsed 30 keV Bi^{3+} (0.16~0.28 pA pulsed current) ion beam was applied for high lateral resolution mapping (< 800 nm) analysis, and typical analysis area was 100 ×100 μm^2, with 1 keV Cs+ ion beam sputtering at the same time(69.27~82.74 nA current), 300 × 300 μm^2 sputter raster.

Soft X-ray absorption spectroscopy (sXAS) measurements

Soft X-ray absorption spectroscopy (sXAS) measurements were carried out at the IOS beamline (23-ID-2) at the National Synchrotron Light Source II (NSLS-II), Brookhaven National Laboratory. Spectra were acquired in partial electron yield (PEY), total electron yield (TEY) and partial fluorescence yield (PFY) modes. The estimated incident X-ray energy resolution was ~0.05 eV at the O K-edge. The monochromator absorption features and beam instabilities were normalized out by dividing the detected PFY and TEY signals by the drain current of a clean gold I0 mesh placed in the incident beam. TEY spectra were recorded from the drain current of the sample and PFY data were acquired using a Vortex EM silicon drift detector. The sXAS spectra for O K-edge were recorded over a wide energy range from 520 to 565 eV covering energies well below and above sample absorptions. The normalization of the O K-edge was performed[1]: 1) I0 normalization: the sample signal is divided by the incident intensity measured from the sample drain current from a freshly coated Au mesh inserted into the beam path before the X-rays can impinge on the sample. 2) A linear, sloping background is removed by fitting a line to the flat low energy region (520-524 eV) of the sXAS spectrum. 3) The spectrum is normalized by setting the flat low energy region to zero and the post-edge to unity (unit edge-jump). The photon energy selected for the post edge was 560 eV, beyond the region of any absorption (peaks).

First-principles density functional theory calculations

We calculated the ground-state crystal structures of $LiCoO_2$ using first-principles density-functional theory [2,3] implemented in the Vienna Ab initio Simulation Package (VASP) [4,5] with the projector-augmented wave method [6] and a plane-wave basis with an energy cutoff of 450 eV. The generalized-gradient approximation of exchange-correlation energy functional in the Perdew-Burke-Ernzerhof [7] form and a Monkhorst-Pack k-point sampling of 8×8×4 for the Brillouin zone integration were adopted. We set the convergence criteria for maximal residual force to 0.005 eV/Å, and the convergence criteria for electronic relaxation to 10^{-6} eV. The Bader charge analysis defined by zero flux surfaces is used [8].

Supplementary References

1 Luo, K. *et al.* Charge-compensation in 3d-transition-metal-oxide intercalation cathodes through the generation of localized electron holes on oxygen. *Nat Chem* **8**, 684-691, doi:10.1038/nchem.2471 (2016).

2 Hohenberg, P. & Kohn, W. Inhomogeneous electron gas. *Physical Review B* **136**, B864-B871, doi:10.1103/PhysRev.136.B864 (1964).

3 Kohn, W. & Sham, L. J. Self-consistent equations including exchange and correlation effects. *Phys. Rev.* **140**, A1133-A1138, doi:10.1103/PhysRev.140.A1133 (1965).

4 Kresse, G. & Furthmüller, J. Efficient iterative schemes for *ab initio* total-energy calculations using a plane-wave basis set. *Physical Review B* **54**, 11169-11186 (1996).

5 Kresse, G. & Furthmüller, J. Efficiency of ab-initio total energy calculations for metals and semiconductors using a plane-wave basis set. *Computational Materials Science* **6**, 15-50 (1996).

6 Blöchl, P. E. Projector augmented-wave method. *Physical Review B* **50**, 17953-17979 (1994).

7 Perdew, J. P., Burke, K. & Ernzerhof, M. Generalized gradient approximation made simple. *Phys. Rev. Lett.* **77**, 3865-3868, doi:10.1103/PhysRevLett.77.3865 (1996).

8 Tang, W., Sanville, E. & Henkelman, G. A grid-based Bader analysis algorithm without lattice bias. *Journal of Physics: Condensed Matter* **21**, 084204 (2009).